Correlations of Chemical, Optical and Structural Properties of Hybrid Perovskites Between Three Different Amino(methyl)pyridine Cations Synthesized with Lead Bromide in Acidic Solution Under Inert Nitrogenized Atmosphere

A. Ramli[1], N. F. Najihah[2], S. R. Hamzah[1], S. Sepeai[3], A. M. M. Ali[2] and W. I. Nawawi[1*]
[1]Faculty of Applied Sciences, Universiti Teknologi MARA, Cawangan Perlis, 02600 Arau, Perlis, Malaysia
[2]Faculty of Applied Sciences, Universiti Teknologi MARA, 40450 Shah Alam, Selangor, Malaysia
[3]Solar Energy Research Institute (SERI), Universiti Kebangsaan Malaysia, 43600 Bangi, Selangor, Malaysia
*Corresponding author (e-mail: wi_nawawi@uitm.edu.my)

Low-dimensional hybrid perovskites have evolved into an interesting platform for optoelectronic applications like solar cells. Despite their widespread use, there has been little investigation of their structure-property correlations. This study aims to elucidate the chemical, optical and structural properties of various dimensional bromoplumbates synthesized under a closed-system nitrogenized atmosphere without using a glove box. Three different amino(methyl)pyridine (AMP) cations (2-AMP, 3-AMP and 4-AMP) were refluxed at 90 °C with lead bromide in hydrobromic acid solution. The precipitate crystals were grown via a solution-cooling process and their chemical, optical and structural properties were determined. FTIR analysis confirmed the presence of NH_3^+, pyridinium and Ar-H ions in the products. The characteristic excitation peaks in the UV-Vis absorption spectra of the [(2-AMP)(3-AMP)(4-AMP)]$PbBr_4$ series were located at 432 nm, 429 nm and 357 nm. The optical bandgap energy values of these compounds were determined using an extrapolated line from the Tauc plot, yielding values of 2.87 eV, 2.89 eV and 3.47 eV. The 4-AMP and [(2-AMP)(3-AMP)]$PbBr_4$ samples exhibited peaks at 467 nm and 468 nm in photoluminescence spectra under emission mode. XRD analysis showed high-order diffraction peaks, indicating the formation of a hybrid crystal with a layered perovskite structure.

Keywords: Amino(methyl)pyridine; hybrid perovskite; low-dimensional; solar cell material.

Received: October 2022; Accepted: January 2023

Hybrid halide perovskites are a promising class of low-cost semiconducting materials that can be employed in a variety of optoelectronic applications such as solar cells [1]–[7], light emitting devices [8]–[13], photo-catalysts [14]–[18], radiation detection [19]–[22], photo- detectors [23]–[25] and lasing [26]–[27]. Perovskite generally refers to a class of compounds with the same crystal structure as calcium titanate ($CaTiO_3$) with the general formula ABX_3, which is also known as the three-dimensional (3D) perovskite structure. A is a monovalent cation such as cesium (Cs^+) or organic cations such as methyl-ammonium ($CH_3NH_3^+$) and formamidinium ($HC(NH_2)_2^+$). The B-site is a divalent metal cation, such as lead (Pb^{2+}) or tin (Sn^{2+}). Mean-while, X represents halide anions such as iodide (I^-), bromide (Br^-), and chloride (Cl^-). Basically, hybrid perovskites consist of anionic B-X-semiconducting frameworks with charge-compensating cations [28]–[29]. The 3D framework is formed by the octahedral metal halide $(BX_6)^{4-}$ via corner-sharing. The site in the middle of the eight-octahedra is occupied by the A cation. Each element must have the proper valence state to meet charge balance requirements.

In the past decades, 3D hybrid halide perovskite materials have been extensively studied due to their remarkable optical and electrical properties such as long carrier diffusion lengths [30]–[32], high absorption coefficients [33]–[34], high defect tolerance [35] and high charge carrier mobility [36]. However, the instability of the 3D perovskite materials against moisture, light and heat was a key challenge that hindered its practical applications in photovoltaic and other optoelectronics devices [37]–[38]. One promising method of suppressing the degradation of 3D perovskite is by lowering the dimension of the structure. According to Li et al., if A cation is too large, the 3D perovskite rule is broken, thus causing the dimension of the inorganic framework to change to 2D, 1D or 0D [39], so-called low-dimensional hybrid perovskites. The BX_6 octahedra in the 2D structure are connected in layered sheets at the corners. In 1D, the BX_6 octahedra are linked in a chain (corner-sharing, edge-sharing, or face-sharing). In contrast, in 0D, the BX_6 octahedra are isolated.

A glove box is a piece of equipment needed during the synthesis-processability of hybrid perovskites.

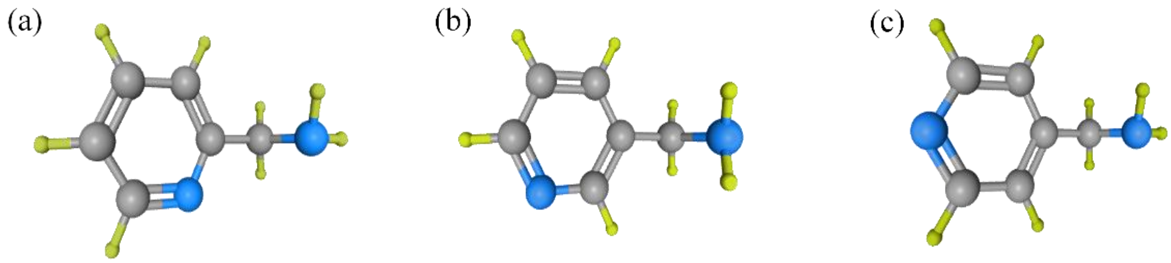

Figure 1. Different locations of the aminomethyl substituent in the pyridine ring (Blue – N atom; Grey – C atom; Green – Hydrogen) of (a) 2-AMP; (b) 3-AMP, and (c) 4-AMP.

However, it has a few disadvantageous such as high operating costs and a large amount of inert gas consumption [40]–[41]. This study builds on different dimensional hybrid perovskites based on different amine ligands. This paper contributes to a new method for synthesizing low-dimensional hybrid perovskites without using a glove box. The hybrid perovskite is formed by the steric interaction of $PbBr_2$ and 2-, 3-, and 4-aminomethylpyridines in a hydrobromic acid solution. The inert nitrogen atmosphere was achieved by directly introducing N_2 gas into the mixture. The as-synthesized hybrid perovskite compounds are referred to as (2-AMP)$PbBr_4$, (3-AMP)$PbBr_4$, and (4-AMP)$PbBr_4$.

EXPERIMENTAL

Materials and Synthesis

Three different amines of 2-amino(methyl)pyridine (2-AMP), 3-amino(methyl)pyridine (3-AMP) and 4-amino(methyl)pyridine (4-AMP) were used as received (Sigma Aldrich, 99%, 108.14 g/mol). These are all cationic amines where the aminomethyl substituent is located at different positions in the pyridine ring, as shown in Fig. 1. The following general procedure was used to synthesize lead bromide $PbBr_4^{2-}$ frameworks with three different $C_6H_8N_2^+$ organic cations in hydrobromic acid solution. Each amine (1 ml) was mixed with 3.67 g of lead (II) bromide ($PbBr_2$) (Sigma Aldrich, 99 %, 367.01 g/mol) in 100 ml HBr acid (Merck, 40 wt%, 80.91 g/mol) in a round bottom flask. To ensure homogeneity, the mixture was swirled for a few seconds. Without a glove box, the nitrogen atmosphere was accomplished by directly introducing N_2 gas into the mixture. It took about 15 minutes to create bubbles in the mixture. Some precipitate was observed in the mixture during this time. After that, the mixture was heat-treated at 90 °C for an hour. The heated mixture was gradually cooled to room temperature. During this time, more solidified precipitate was formed in the flask. The yellowish-white precipitate was isolated from each solution through filtration. Subsequently, these were dried using an assisted vacuum-pump and labelled as (2-AMP)$PbBr_4$, (3-AMP)$PbBr_4$ and (4-AMP)$PbBr_4$.

Characterization

Infrared spectra of all samples were recorded using the KBr pellet method in the 400 – 4000 cm^{-1} range with a Perkin-Elmer Frontier Fourier Transform Infrared (FT-IR) spectrophotometer. Absorbance spectra were measured within an integrating sphere on a Perkin Elmer Lambda 950 UV-Vis-NIR spectrometer. The emission spectra were taken on an Edinburgh Instrument FLS920 photoluminescence (PL) spectrometer equipped with a 450 W xenon lamp as the excitation source. X-ray diffraction was performed with a PANanalytical X'Pert Pro diffractometer using Cu-Kα (λ= 0.15405 nm) radiation. Structural refinement of all samples was carried out using the General Structure Analysis System (GSAS) program, and EXPGUI package crystal structures [42]–[43] were visualized using VESTA software [44]. Microstructure images were obtained by a Zeiss Supra 55VP field emission scanning electron microscope (FESEM). Energy-dispersive X-ray (EDX-Model X-Max^N) measurements were used to determine the elemental composition of each sample.

RESULTS AND DISCUSSION

Chemical Properties

Weak infrared (IR) bands centred at 3113 cm^{-1}, 3119 cm^{-1} and 3121 cm^{-1} in Fig. 2 can be assigned to the stretching of the N-H amide. A group of bands in the region 1578 – 1632 cm^{-1} in the IR spectra of all samples indicate the characteristic stretching of the (C=N) and (C=C) aromatic groups, revealing the presence of organic ligands. There are similarities in the deformation and elongation vibrations of the NH_3^+ group between the present study and those described by Hamdi et al. [45] for the protonation of the 2-picolyamine molecule around 1500 and 3110 cm^{-1}. For all samples, the C-H alkyl groups displayed a prominent bending peak at 1400 cm^{-1}. The mono-substituted aromatic C-H bond gave a noticeable signal between 675 – 773 cm^{-1} in the IR fingerprint region due to the vibrations of the amine group.

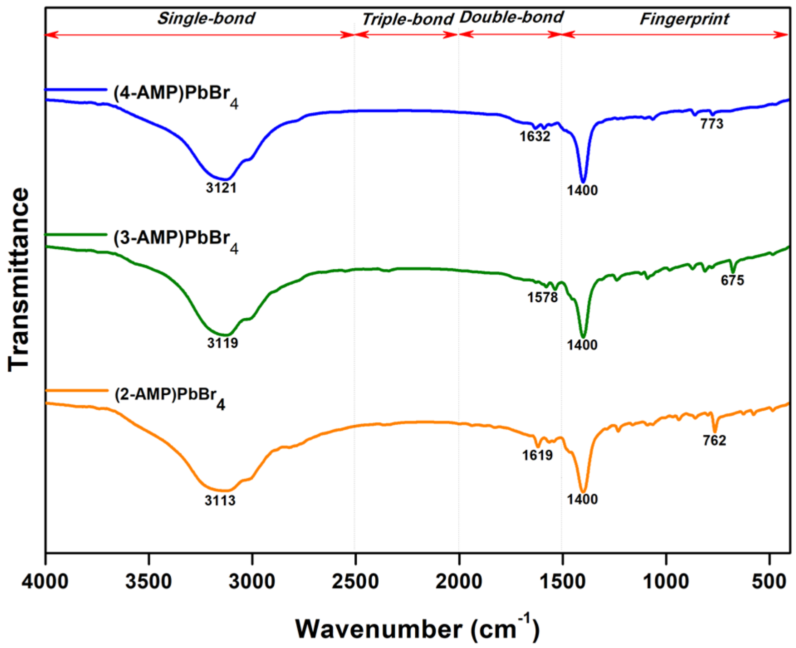

Figure 2. FT-IR spectra of (2-AMP)$PbBr_4$, (3-AMP)$PbBr_4$ and (4-AMP)$PbBr_4$.

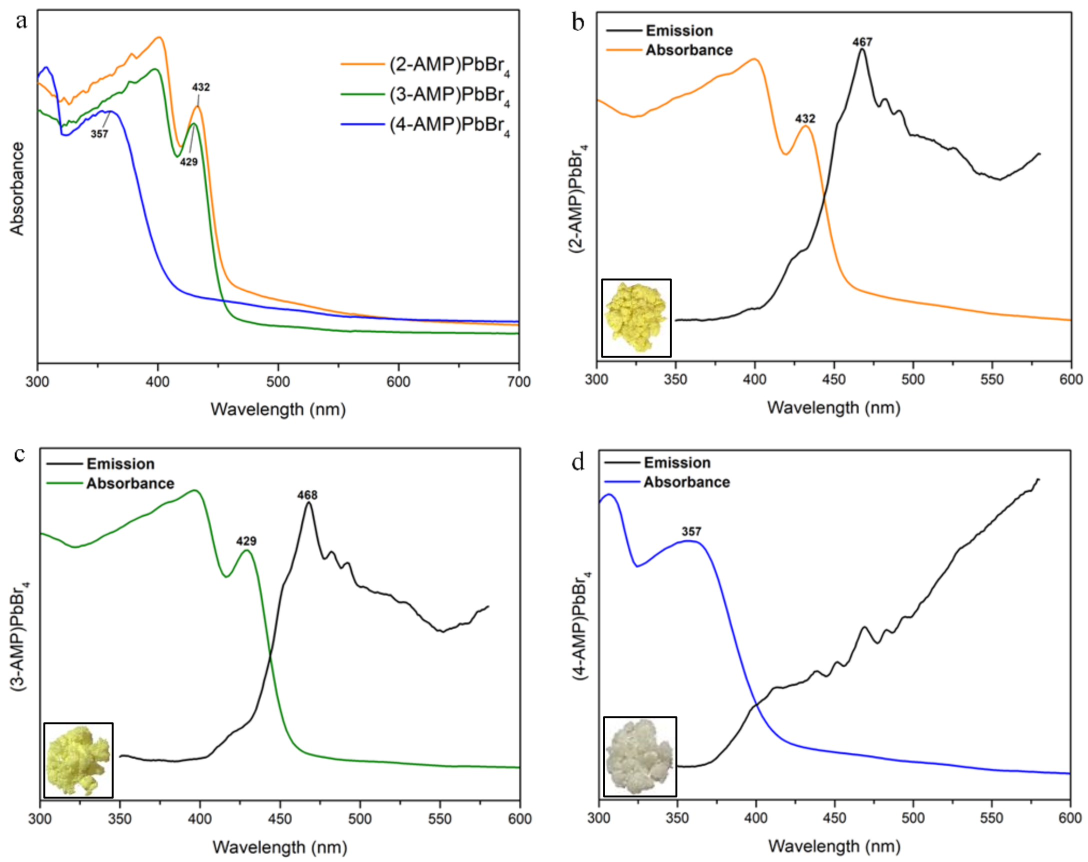

Figure 3. (a) UV-Vis absorption spectrum; (b) – (d) Emission-absorbance spectra for (2-AMP)$PbBr_4$, (3-AMP)$PbBr_4$ and (4-AMP)$PbBr_4$.

Optical Properties

Fig. 3 depicts the absorbance and emission profiles of all the samples. The insets in Fig. 3 (b)-(d) displays the appearance of the synthesized crystals. The PL spectra of the (2-AMP)$PbBr_4$ and (3-AMP)$PbBr_4$ samples exhibited one prominent peak immediately upon excitation. Peaks at 467 nm in (2-AMP)$PbBr_4$ and 468 nm in (3-AMP)$PbBr_4$ indicate the excitation emission characteristics of the $PbBr_4^{2-}$ inorganic layer. In contrast, no prominent peak was detected for the (4-AMP)$PbBr_4$ sample. The PL peak near the absorption maximum was attributed to band-to-band recombination. The Stokes shift values were 35 nm and 39 nm for (2-AMP)$PbBr_4$ and (3-AMP)$PbBr_4$, respectively. For the (4-AMP)$PbBr_4$ sample, no Stokes shift could be calculated as the emission spectrum did not display any prominent peaks. Electronic transitions within the inorganic layer cause luminescence. Hybrid perovskite is a semiconductor quantum well structure with small band gap inorganic sheets (quantum-carriers) alternating with larger band gap organic layers (wells).

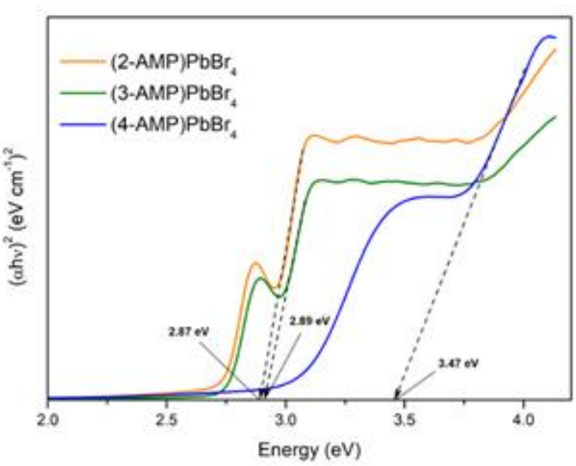

Figure 4. Tauc plot fitted to the band edge for (2-AMP)$PbBr_4$, (3-AMP)$PbBr_4$ and (4-AMP)$PbBr_4$.

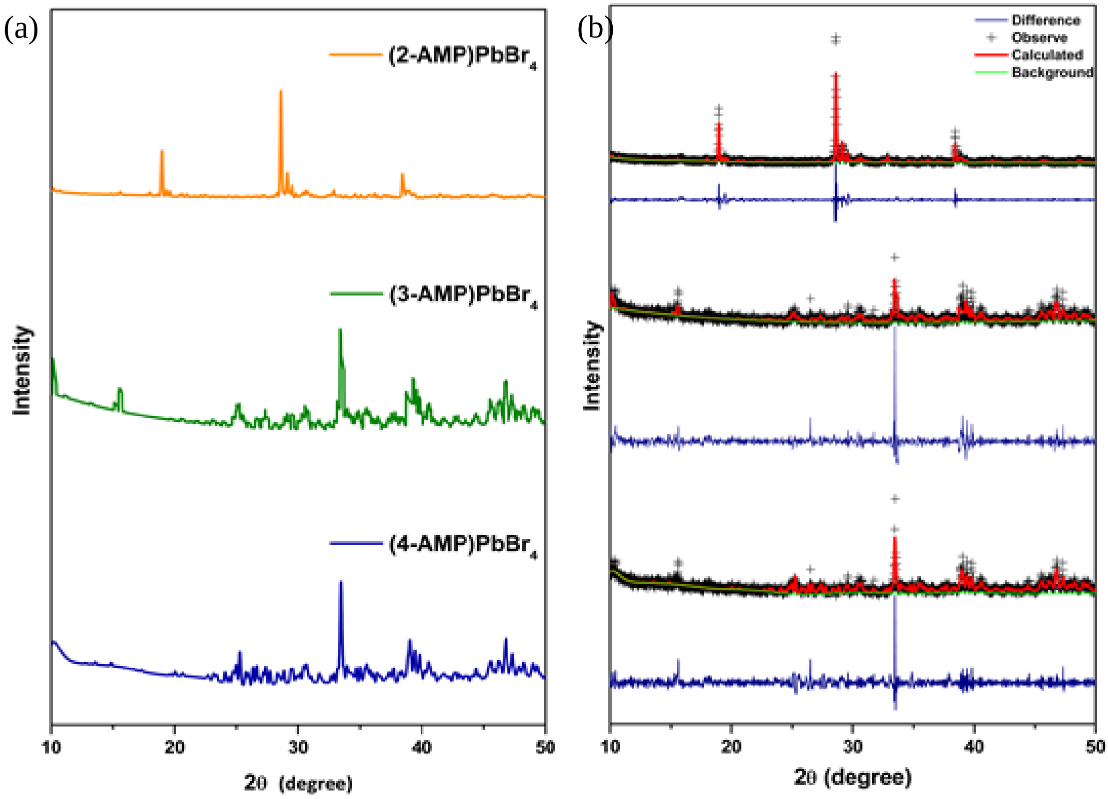

Figure 5. (a) X-ray diffraction patterns and (b) Final Refinements for (2-AMP)$PbBr_4$, (3-AMP)$PbBr_4$ and (4-AMP)$PbBr_4$.

The optical band gap was determined by extrapolating the linear region to the X-axis intercept using a Tauc plot of $(\alpha h\nu)^{1/n}$ versus energy gap E_g (eV). As in Fig. 4, the $n = 1/2$ plot shows a linear Tauc region above the optical absorption edge for a direct band gap semiconductor, whereas the $n = 2$ plot shows a Tauc region for an indirect band gap material. The extrapolated line of the edge of the Tauc plot gave band gap values of 2.87 eV and 2.89 eV for (2-AMP)$PbBr_4$ and (3-AMP)$PbBr_4$, respectively. The slightly higher value of E_g ~ 3.47 eV was obtained for the (4-AMP)$PbBr_4$ sample because the excitation peak in the absorption spectra was observed at a lower wavelength of 357 nm. The obtained band gap value was quite close to the reported band gap of the corrugated 2D lead bromide compounds of -(DMEN) $PbBr_4$ (~ 3 eV), (DMAPA)$PbBr_4$ (~ 2.88 eV), and (DMABA)$PbBr_4$ (~ 2.85 eV) synthesized under N_2 [46].

Structural Properties

Fig. 5 illustrates the X-ray diffraction (XRD) patterns of all the samples. The diffraction peaks of the three samples (2-AMP)$PbBr_4$, (3-AMP)$PbBr_4$, and (4-AMP) $PbBr_4$ were well-defined and evenly-spaced. The XRD data from all samples were refined using the Rietveld method to obtain lattice parameters and unit cell sizes. During the refinement, a diffraction profile for the proposed structure was calculated and compared to the experimental XRD data. The proposed structure was then refined using a least-squares approach to generate a best-fit model structure by adjusting parameters of the proposed structure to reduce the differences between experimental and calculated intensities. The final refinement values of the structural parameters, bond lengths, bond angles and chi-squares (χ^2) for all samples are listed in Tables 1 and 2.

The orthorhombic Pbca space group structure of (2-AMP)$PbBr_4$ was crystalline, with unit cell dimensions of a = 17.3955 (6) Å, b = 8.2431 (3) Å, and c = 18.7239 (3) Å. The crystal structure exhibited a staggered, periodic stacking of layers along the crystallographic c-axis (Fig. 6a). $PbBr_2^{2-}$ 2-AMP cations separated the layers in two different directions, and adjacent inorganic layers were connected by charge-assisted hydrogen bonding. This perovskite's octahedron was slightly distorted, with Br-Pb-Br bond angles varying from 88.70 (3)° to 97.6 (3)° and Pb-Br band lengths between 2.9484 (8) Å and 3.0888 (8) Å (Table 2). In the ab-plane, corner-sharing octahedra compensated for the perovskite-type layer. The organic cations played a suitable role in ionic bonding, steric hindrance, and hydrogen bonding to fit the coordination environment due to the confinement of the inorganic layers.

Compound (3-AMP)$PbBr_4$ belonged to the same space group as 2-AMP-based compounds but had smaller lattice parameters, as shown in Table 1, with a = 16.1262 (5), b = 8.2180 (5), and c = 18.0629 (4) Å. In Fig. 6, the Pb atom enacted octahedral geometry and formed isolated octahedrons, with the bond length of Pb-Br ranging from 3.071 (14) to 3.169 (6) Å and the bond angle of Br-Pb-Br in octahedrons ranging from 88.32 (27) to 91.68 (27) ° (Table 2). This was an ideal octahedron representing the non-stereochemical activity of the lone pair of electrons of lead (II). Each layer of isolated $PbBr_6^{2-}$ octahedrons was tilted in a different direction, alternating along the a-axis.

In contrast, (4-AMP)$PbBr_4$ had a monoclinic crystal structure with the space group $P2_{1/c}$. As shown in Fig. 6, the octahedron in (4-AMP)$PbBr_4$ was more distorted than the octahedron in (2-AMP)$PbBr_4$, resulting in a zigzag edge-sharing octahedral $PbBr_4^{2-}$ chain. Pb-Br bond lengths ranged from 2.8637 (14) to 3.1526 (16) Å, and Br-Pb-Br bond angles ranged from 84.07 (4) to 97 (4) ° (Table 2). This indicated that the lone pair of electrons of lead (II) in (4-AMP)$PbBr_4$ were stereochemically active, despite being synthesized under the same conditions as the other two compounds.

Table 1. Crystal structure parameters of (2-AMP)$PbBr_4$, (3-AMP)$PbBr_4$ and (4-AMP)$PbBr_4$.

Compound	Crystal System	Space Group	Lattice parameter (Å)			Volume (Å^3)	Goodness of Fit	Others Ref.
			a	b	c	V	χ^2	
(2-AMP)$PbBr_4$	Orthorhombic	Pbca	17.3955 (6)	8.2431 (3)	18.7239 (3)	2684.87	1.610	
	Orthorhombic	Pbca	17.400	8.2406	18.733	2686.1		[47]
	Orthorhombic	Pbca	17.3765	8.2397	18.7056			[48]
(3-AMP)$PbBr_4$	Orthorhombic	Pbca	16.1262 (5)	8.2180 (5)	18.0629 (4)	2393.78	1.561	
	Orthorhombic	Pbca	15.788	8.146	17.215	2213.9		[47]
(4-AMP)$PbBr_4$	Monoclinic	$P2_1/c$	12.3918 (6)	13.8325 (9)	7.9189 (4)	1307.99	1.438	
	Monoclinic	$P2_1/c$	12.3851	13.8278	7.9202	1307.30		[47]
	Monoclinic	$P2_1/c$	12.390	13.824	7.927	1308.5	1.293	[49]

The structure of (4-AMP)$PbBr_4$ showed evident layer formation, with organic cations and inorganic chains arranged in a regular structure. The steric hindrance and hydrogen bonding confinement between the organic ammonium hydrogen ions and halides in the inorganic chains dictated chain packing.

Although the three very similar organic amines of 2-AMP, 3-AMP and 4-AMP coordinated with inorganic-bromohalide $PbBr_2$ under the same synthesis conditions, the obtained $PbBr_2$ frameworks differed from each other. The conformations of the three ligands in all the compounds are shown in Fig. 7. All of the atoms in the pyridine ring, as well as the first methyl-ammonium carbon attached to the benzene ring, can be seen in the three ligands. For each of the compounds (2-AMP)$PbBr_4$, (3-AMP)$PbBr_4$, and (4-AMP)$PbBr_4$, the bending angles of methylammonium were C5-C6-N1:110.86 (2), C1-C2-N1:114.85 (24) and C1-C2-N1:115.22 (4) °, respectively. There are similarities between the imposed distortion angles in the present study and those described by L. Mao et al., indicating that the nature of the spacer cations influences the interlayer separation of the inorganic framework [50].

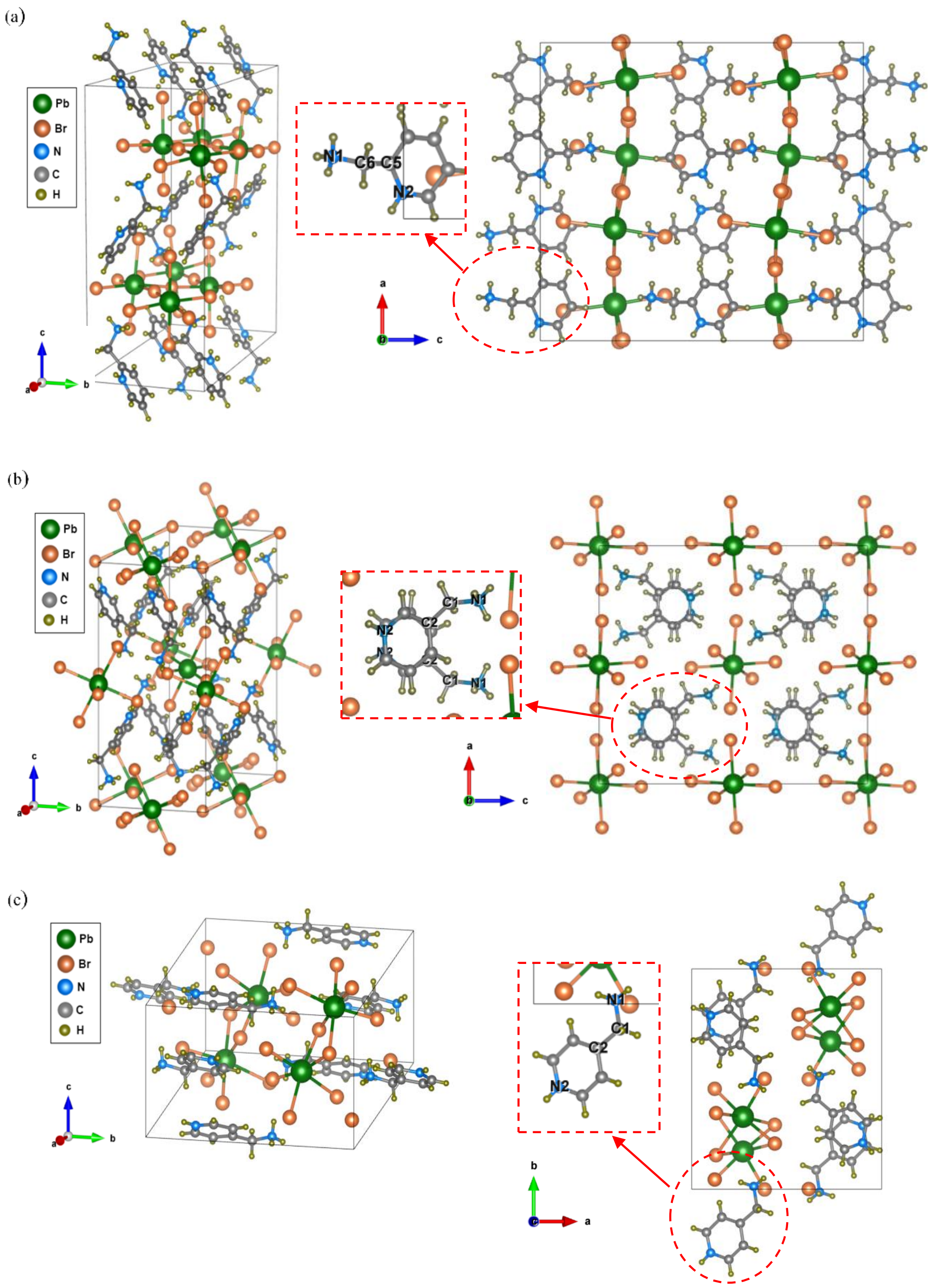

Figure 6. Crystal packing structure of (a) (2-AMP)$PbBr_4$, (b) (3-AMP)$PbBr_4$ and (c) (4-AMP)$PbBr_4$ with hydrogen bonds.

Table 2. Selected bond lengths [Å] and angles [°].

Compound	Bond length (Å)	Bond angle (°)	Y. Li et al. [47]
(2-AMP)PbBr$_4$			
Pb1_Br3	2.9484 (8)		2.9483
Pb1_Br2	2.9889 (8)		2.9887
Pb1_Br4	3.0071 (6)		3.009
Pb1_Br2	3.0888 (8)		3.0890
Pb1_Br3	3.0217 (8)		3.0218
Br3_Pb1_Br2		88.70 (3)	88.73
Br3_Pb1_Br4		91.24 (1)	91.25
Br1_Pb1_Br2		81.06 (0)	81.06
Br2_Pb1_Br2		85.80 (3)	85.771
Br3_Pb1_Br2		97.60 (3)	97.63
N1_C6_C5		110.86 (2)	111
(3-AMP)PbBr$_4$			
Pb1_Br1	3.169 (6)		3.0444
Pb1_Br2	3.123 (9)		3.0604
Pb1_Br3	3.071 (14)		3.0206
Br3_Pb1_Br1		91.68 (27)	93.38
Br3_Pb1_Br1		88.32 (27)	86.62
Br3_Pb1_Br2		90.25 (21)	90.048
Br1_Pb1_Br2		88.65 (9)	88.260
Br3_Pb1_Br2		89.75 (21)	89.952
Br1_Pb1_Br2		91.35 (9)	91.74
N1_C1_C2		114.85 (24)	113.3
(4-AMP)PbBr$_4$			
Pb1_Br1	2.9276 (14)		2.9278
Pb1_Br2	2.8637 (14)		2.8632
Pb1_Br3	3.0151 (15)		3.0135
Pb1_Br3	3.1526 (16)		3.1530
Pb1_Br4	3.0389 (16)		3.0377
Pb1_Br3_Pb1		94.19 (4)	94.22
Br2_Pb1_Br1		86.40 (5)	86.43
Br1_Pb1_Br3		97.00 (4)	96.97
Br2_Pb1_Br4		88.06 (3)	88.04
Br1_Pb1_Br4		92.81 (4)	92.85
Br3_Pb1_Br3		84.07 (4)	84.10
N1_C1_C2		115.22 (4)	115.2

Morphological Analysis

The morphological structures of the (2-AMP)PbBr$_4$, (3-AMP)PbBr$_4$, and (4-AMP)PbBr$_4$ hybrid perovskite crystals were confirmed by FESEM analysis, while the elemental composition of each sample was analysed by EDX, the results of which are shown in Fig. 7. All samples contained the major elements Br, Pb, C and N, as well as the minor elements O, Al, Ag and Cu. It was impossible to deconvolute the EDX bromine-line (1.48 keV) and aluminium K-line from the peak for all samples (1.48 keV). Al appeared as a weak feature in the spectra due to the sample holder used for the measurements. All samples had a needle-like morphology due to the Pb-rich phase [48].

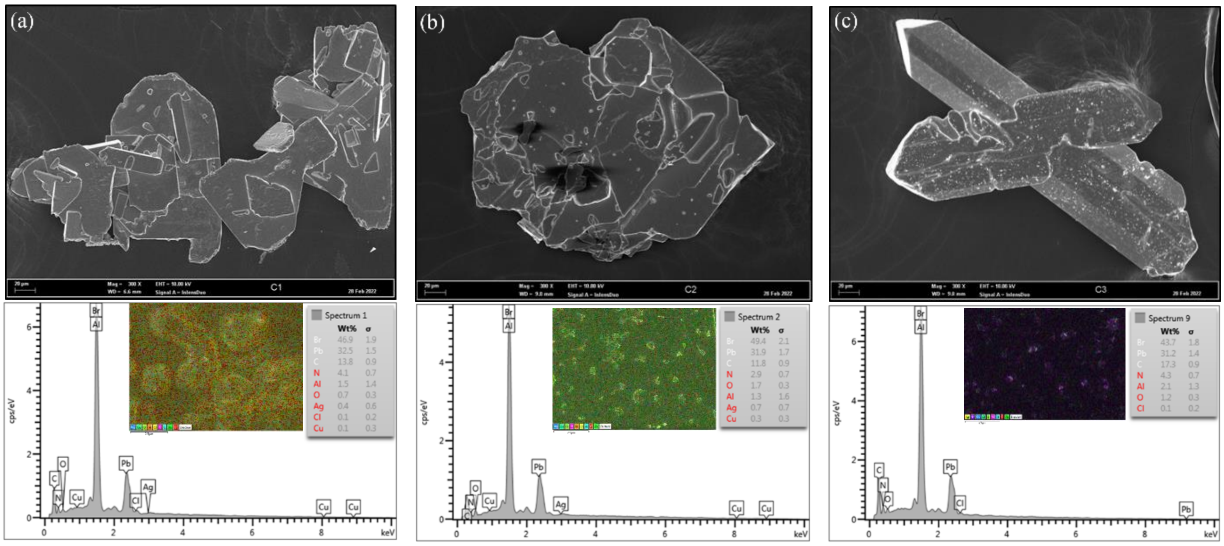

Figure 7. The morphology and EDX analysis of (a) (2-AMP)$PbBr_4$, (b) (3-AMP)$PbBr_4$ and (c) (4-AMP)$PbBr_4$ hybrid perovskites.

CONCLUSION

In conclusion, we have discovered a new method for successfully synthesizing hybrid perovskites using three different organic ligands of amino(methyl)pyridine by reaction with inorganic lead bromide under a nitrogen atmosphere without the use of a glove box. The chemical, optical and structural properties of the as-synthesized layered haloplumbate products displayed different $PbBr_2$ framework dimensions when ligands with different aminomethyl substituent positions on the pyridine ring were used. The optical absorption properties and low energy gap (E_g) values of (2-AMP)$PbBr_4$ and (3-AMP)$PbBr_4$ stood out among these three compounds, indicating that they can potentially be used to integrate low-dimensional lead bromide perovskites in optoelectronic devices.

ACKNOWLEDGEMENTS

The authors are grateful to the Ministry of Higher Education (MOHE) Malaysia for their financial support via the Fundamental Research Grant Scheme (FRGS) (File No: FRGS/1/2021/STG07/UITM/02/7) and Universiti Teknologi MARA for the facilities and support.

REFERENCES

1. Maiti, A., Chatterjee, S., Peedikakkandy, L. and Pal, A. J. (2020) Defects and their Passivation in Hybrid Halide Perovskites towards Solar Cell Applications. *Sol. RRL*.

2. Jan, F., *et al.* (2021) Structural and optoelectronic properties of hybrid halide perovskites for solar cells. *Org. Electron.*, **91**, January, 106077.

3. García-fernández, A., *et al.* (2018) Benchmarking Chemical Stability of Arbitrarily Mixed 3D Hybrid Halide Perovskites for Solar Cell Applications. *Small Methods*, **1800242**, 1–8.

4. Vidyasagar, C. C. and Mun, B. M. (2018) Recent Advances in Synthesis and Properties of Hybrid Halide Perovskites for Photovoltaics. *Nano-Micro Lett.*, **5**.

5. C. A. O. and G. G. Migueal A. Reinoso (2019) Improvement Properties of Hybrid Halide Perovskite Thin Films Prepared by Sequential Evaporation for Planar Solar Cells. *Materials (Basel).*, **12**, 1394.

6. Dey, P., Singh, H., Gupta, R. K., Goswami, D. and Maiti, T. (2020) Journal of Physics and Chemistry of Solids Organic-inorganic hybrid halide perovskites impregnated with Group 1 and 15 elements for solar cell application. *J. Phys. Chem. Solids*, **144**, April, 109518.

7. Wang, M., Li, B., Siffalovic, P., Chen, L. -C., Cao, G. and Tian, J. (2018) Monolayer-like Hybrid Halide Perovskite Films Prepared by Additive Engineering without Antisolvent for Solar Cells. *J. Mater. Chem. A.*, **31**.

8. Liu, X., *et al.* (2020) Metal halide perovskites for light-emitting diodes. *Nat. Mater.*, **20**, 10–21,

9. Jaramillo-quintero, O. A., Sánchez, R. S., Rincón, M. and Mora-sero, I. (2015) Bright Visible-Infrared Light Emitting Diodes Based on Hybrid Halide Perovskite with Spiro-OMeTAD as a Hole Injecting Layer Bright Visible-Infrared Light Emitting

Diodes Based on Hybrid Halide Perovskite with Spiro-OMeTAD as a Hole Injecting Layer. *J. Phys. Chem. Lett.*, **6**, 1883–1890.

10. Andricevic, P., Mettan, X., Sienkiewicz, A., Garma, T. and Rossi, L. (2019) Light-Emitting Electrochemical Cells of Single Crystal Hybrid Halide Perovskite with Vertically Aligned Carbon Nanotubes Contacts. *ACS Photonics*, **6**, 967–975.

11. Ayguler, M. F., Weber, M. D., Puscher, B. M. D., Medina, D. D. and Docampo, P. (2015) Light-Emitting Electrochemical Cells Based on Hybrid Lead Halide Perovskite Nanoparticles. *J. Phys. Chem. Lett.*, **119**, 12047–12054.

12. Innocenzo, V. D., Ram, A., Kandada, S., De Bastiani, M., Gandini, M. and Petrozza, A. (2014) Tuning the Light Emission Properties by Band Gap Engineering in Hybrid Lead Halide Perovskite. *J. Am. Chem. Soc.*, **136**, 17730–17733.

13. Smith, M. D. and Karunadasa, H. I. (2018) White-Light Emission from Layered Halide Perovskites. *Acc. Chem. Res.*, **51**, 619–627.

14. Zhu, X., Lin, Y., Sun, Y., Beard, M. C. and Yan, Y. (2019) Lead-Halide Perovskites for Photo-catalytic α-Alkylation of Aldehydes. *J. Am. Chem. Soc.*, **141**, 733–738.

15. Aamir, M., Hussain, Z., Sher, M. and Iqbal, A. (2017) Enhanced photocatalytic activity of water stable hydroxyl ammonium lead halide perovskites. *Mater. Sci. Semicond. Process.*, **63**, 6–11.

16. Huang, H., *et al.* (2018) Efficient and Selective Photocatalytic Oxidation of Benzylic Alcohols with Hybrid Organic-Inorganic Perovskite Materials. *ACS Energy Lett.*, **755–759**.

17. Kong, W., Rahimi-iman, A., Bi, G., Dai, X. and Wu, H. (2016) Oxygen Intercalation Induced by Photocatalysis on the Surface of Hybrid Lead-Halide Perovskites. *J. Phys. Chem. C.*, **120,** 7606–7611.

18. Zhao, Z., *et al.* (2019) Applied Catalysis B : Environmental Stable hybrid perovskite MAPb (I1 − xBrx)3 for photocatalytic hydrogen evolution. *Appl. Catal. B Environ.*, **253**, 41–48.

19. Kakavelakis, G., Gedda, M., Panagiotopoulos, A., Kymakis, E., Anthopoulos, T. D. and Petridis, K. (2020) Metal Halide Perovskites for High-Energy Radiation Detection. *Adv. Sci.*, **2002098**, 1–33.

20. Wei, H. and Huang, J. (2019) Halide lead perovskites for ionizing radiation detection. *Nat. Commun.*, 1–12.

21. Ji, C., *et al.* (2019) 2D Hybrid Perovskite Ferro-electric Enables Highly Sensitive X-Ray Detection with Low Driving Voltage. *Adv. Funct. Mater.*, **1905529**, 1–7.

22. Wang, X., *et al.* (2020) Solution-Processed Halide Perovskite Single Crystals with Intrinsic Compositional Gradients for X-Ray Detection. *Chem. Mater.*, **32**, 4973–4983.

23. Yu, X., Tsao, H. N., Zhang, Z. and Gao, P. (2020) Miscellaneous and Perspicacious : Hybrid Halide Perovskite Materials Based Photodetectors and Sensors. *Adv. Opt. Mater.*, **2001095**, 1–23.

24. Ding, J., Cheng, X., Jing, L, Zhou, T., Zhao, Y. and Du, S. (2017) Polarization-Dependent Opto-electronic Performances in Hybrid Halide Perovskite MAPbX3 (X = Br , Cl) Single Crystal Photo-detectors. *Appl. Mater. Interfaces*, **10**, 845–850.

25. Ji, L., Hsu, H., Lee, J., Bard, A. J. and Yu, E. T. (2018) High performance photodetectors based on solution- processed epitaxial grown hybrid halide perovskites. *Nano Lett.*, **18**, 994–1000.

26. Udalova, N. N., Tutantsev, A. S., Chen, Q., Kraskov, A., Goodilin, E. A. and Tarasov, A. B. (2020) New Features of Photochemical Decomposition of Hybrid Lead Halide Perovskites by Laser Irradiation. *Appl. Mater. Interfaces*, **12**, 12755–12762.

27. Schünemann, S., Brittman, S., Chen, K., Garnett, E. C. and Tüysüz, H. (2017) Halide Perovskite 3D Photonic Crystals for Distributed Feedback Lasers. *ACS Photonics*, **4**, 2522–2528,

28. González-carrero, S., Galian, R. E. and Pérez-prieto, J. (2015) Organometal Halide Perovskites : Bulk Low-Dimension Materials and Nanoparticles.

29. Li, D., Shi, J., Xu, Y., Luo, Y. and Wu, H. (2018) Inorganic–organic halide perovskites for new photo-voltaic technology. **5**59–576.

30. Lim, J., *et al.* (2022) Long-range charge carrier mobility in metal halide perovskite thin-films and single crystals via transient photo-conductivity. **1–9**.

31. Ma, J. and Wang, L. (2015) Nanoscale Charge Localization Induced by Random Orientations of Organic Molecules in Hybrid Perovskite CH 3 NH 3 PbI 3.

32. Bai, S., Wu, Z., Song, T. and Liu, R. (2014) High-performance planar heterojunction perovskite solar cells : Preserving long charge carrier diffusion lengths and interfacial engineering. June.

33. Li, X., *et al.* (2020) “Three-Dimensional Lead

Iodide Perovskitoid Hybrids with High X - ray Photoresponse.

34. Akinlami, R. O. A. J. O. and Adebayo, T. A. A. G. A. (2019) Unraveling the Stable Phase, High Absorption Coefficient, Optical and Mechanical Properties of Hybrid Perovskite - CH 3 NH 3 Pb x Mg 1 – x I 3 : Density Functional Approach. *J. Inorg. Organomet. Polym. Mater.*, no. 0123456789.

35. Zhang, Y., *et al.* (2019) Nano Energy Auto-passivation of crystal defects in hybrid imidazolium /methylammonium lead iodide films by fumigation with methylamine affords high efficiency perovskite solar cells. *Nano Energy*, **58**, January, 105–111.

36. Zhang, H., *et al.* (2020) Influence of Functional Diamino Organic Cations on the Stability, Electronic Structure, and Carrier Transport Properties of Three- Dimensional Hybrid Halide Perovskite.

37. Park, B. and Il Seok, S. (2019) Intrinsic Instability of Inorganic – Organic Hybrid Halide Perovskite Materials. **1805337**, 1–17,

38. Zhou, Y. (2019) Environmental Science Chemical stability and instability of inorganic halide perovskites. **1**.

39. Li, X., Ho, J. M. and Kanatzidis, M. G. (2021) The 2D Halide Perovskite Rulebook : How the Spacer Influences Everything from the Structure to Optoelectronic Device Efficiency.

40. Zhang, Y., *et al.* (2021) Ambient Fabrication of Organic–Inorganic Hybrid Perovskite Solar Cells. *Small Methods*, **5**, 1, 1–40.

41. Krishna, B. G., Sundar, D. and Tiwari, S. (2021) Progress in ambient air-processed perovskite solar cells : Insights into processing techniques and stability assessment. *Sol. Energy*, **224**, May, 1369–1395.

42. Toby, B. H. (2001) EXPGUI, a graphical user interface for GSAS, 210–213.

43. Toby, B. H. and Von Dreele, R. B. (2013) "GSAS-II : the genesis of a modern open-source all purpose crystallography software package, 544–549.

44. Momma, K. and Izumi, F. (2008) VESTA : a three-dimensional visualization system for electronic and structural analysis, 653–658.

45. Hamdi, I., Bkhairia, I., Roodt, A., Nasri, M. and Roisnel, T. (2020) Synthesis, intermolecular interactions and biological activities of two new organic–inorganic hybrids C6H10N2,2Br and C6H10N2,2Cl.H2O. *R. Soc. Chem.*, **10**, 5864–5873.

46. Lingling, M., Wu, Y., Stoumpos, C. C., Michael, W. R. and Kanatzidis, M. G. (2017) White-Light Emission and Structural Distortion in New Corrugated Two-Dimensional Lead Bromide Perovskites. *J. Am. Chem. Soc.*, **139**, 14, 5210–5215.

47. Li, Y., Zheng, G., Lin, C. and Lin, J. (2007) Synthesis, structure and optical properties of different dimensional organic-inorganic perovskites. *Solid State Sci.*, **9**, 9, 855–861, Sep.

48. Lermer, C., *et al.* (2018) Completing the Picture of 2-(Aminomethylpyridinium) Lead Hybrid Perovskites: Insights into Structure, Conductivity Behavior, and Optical Properties. *Chem. Mater.*, **30**, 18, 6289–6297.

49. Jung, M. (2020) Broadband white light emission from one-dimensional zigzag edge-sharing perovskite, 171–180,

50. Mao, L., *et al.* (2020) Organic Cation Alloying on Intralayer A and Interlayer A' sites in 2D Hybrid Dion − Jacobson Lead Bromide Perovskites (A')(A)Pb2 Br7. *J. Am. Chem. Soc.*, **142**, 8342–8351.